



Carrier synergistic effect of iron based catalysts for CO hydrogenation to lower olefins

Zhenxin Liu¹ · Huiwen Liu¹ · Yuji Gao¹ · Yu Xing¹

Received: 25 October 2023 / Accepted: 11 December 2023 / Published online: 10 February 2024
© Akadémiai Kiadó, Budapest, Hungary 2024

Abstract

Three types of catalyst samples, namely alumina carried Fe/K, zinc aluminate carried Fe/K, and (zinc aluminate + alumina) composite carried Fe/K, were prepared under calcination conditions of 350 °C. The catalysts were characterized by XRD, ICP-OES, N₂ physical adsorption, field emission electron microscopy as well as CO₂-TPD. The performances of the catalysts in CO hydrogenation were tested in a fixed bed reactor. The results show that under similar conversions, the C₂=–C₄= hydrocarbon selectivity of the prepared (zinc aluminate + alumina) composite carried Fe/K catalyst can reach 5 times that of the prepared alumina carried Fe/K catalyst and 9 times that of the prepared zinc aluminate carried Fe/K catalyst, exhibiting a typical synergistic effect based on carrier composition. The basis for this synergistic effect is the significant difference in base sites on the catalyst surface.

Keywords Syngas · Hydrogenation · Catalyst · Lower olefins

Introduction

Syngas is a type of mixed gas (including carbon monoxide and hydrogen) that can be produced by reforming and processing carbon containing raw materials (such as coal, biomass, natural gas, etc.), and further adjusting the composition ratio of the mixed gas through processes such as water–gas shift [1, 2]. Through the catalytic conversion of syngas, which is the implementation of CO hydrogenation, also known as Fischer Tropsch synthesis, it can be used to produce many important basic organic chemical raw materials, greatly reducing the dependence on petroleum [3–6]. The products of CO hydrogenation include gasoline, diesel, kerosene, wax, alcohol, ether, lower olefins, etc. The selectivity of the products mainly depends on the type of catalyst and specific process conditions such as space velocity, temperature, and total pressure [7–10].

✉ Yu Xing
yuxing@zzuli.edu.cn

¹ Henan Provincial Key Laboratory of Surface and Interface Science, School of Materials and Chemical Engineering, Zhengzhou University of Light Industry, Zhengzhou 450002, China

Lower olefins usually refer to short carbon chain olefins such as ethylene, propylene, and butene, written as “C₂–C₄” [10]. Syngas can be used to indirectly produce lower olefins or directly to produce lower olefins. The direct Fischer–Tropsch to lower olefins (FTO) synthesis process has three main types of catalysts: iron based [11–13], cobalt based [14], and oxide/zeolite based [15–17].

The Na/S modified catalyst of K.P. de Jong’s group is an extremely important achievement in iron-based FTO catalysts [11, 12]. However, Na/S promoter has a certain degree of water solubility, and in the CO hydrogenation process, water vapor is an inevitable product, so there is a risk of Na/S promoter being lost [18, 19]. Therefore, it is necessary to further develop iron based FTO catalysts that can withstand water vapor environments and are not prone to loss of promoters [18, 19].

Composite oxides (such as AB₂O₄ spinels) typically have excellent characteristics such as adjustable properties, few losses of composition, and resistance to water vapor. The performance of zinc-containing composite oxide carriers in cobalt-based and iron-based CO hydrogenation catalysts has gradually received attentions [18–20]. The application of composite oxides in FTO reactions mainly involves two major combinations: one is the combination of zeolite molecular sieves and composite oxides [15]; the second is the combination of iron and composite oxides [13, 18]. These two major combinations have made considerable progress in the field of FTO, and Zn element has indeed become a key element in the composite oxide composition of FTO catalysts [13, 15, 18].

For FTO catalysts, if NaHCO₃ is employed as the precipitant in the carrier preparation process, although some catalysts have good performance, this sodium-containing precipitant can also cause different sodium content in the sediment of each reactor’s carrier. This is because sodium ions have variable adsorption capacity, and no matter how they are washed and filtered, they cannot be completely washed or simply fixed at a specific content [18–20]. In addition, if high temperatures such as 1200 °C are used in a study, the crystalline phases in the carrier will also be quite complicated [18, 19]. Therefore, in this study, in order to eliminate the interference of different sodium contents and high-temperature calcination, ammonium type compound ((NH₄)₂CO₃) (rather than NaHCO₃) was used as the precipitant in the preparation processes of different carriers, and the calcination of the carriers was also set to a mild temperature of 350 °C. This method was used to specifically explore the influence of carrier components on the FTO catalytic performance of Fe/K catalyst samples. Due to the overly strong alkalinity of ZnO found in previous investigation, which is not suitable for CO hydrogenation [21], the ZnO carrier was not included in this study.

Experimental section

Preparation of samples

The composition of a sample is represented by the nominal composition of the elements. The iron (Fe) in the sample composition is the active center (during the reaction process, iron may undergo some degree of carbonization, generating

iron carbide [10]). K_2O in the sample composition is used as a promoter [10]. The Al_2O_3 , $ZnAl_2O_4$, $ZnAl_2O_4 \cdot Al_2O_3$ in the sample composition represent the nominal composition of different carriers.

Preparation of sample A1 (i.e. $15\%Fe + 2\%K_2O + 83\%Al_2O_3$, mass fraction, the same below): Weigh $Al(NO_3)_3 \cdot 9H_2O$ and precipitant $(NH_4)_2CO_3$, and dissolve them in deionized water to form two solutions. Drop these two solutions into water simultaneously at $40\text{ }^\circ C$ and stirring conditions to undergo precipitation reaction. Wash thoroughly after suction filtration. After partially dehydrating the filter cake in an $80\text{ }^\circ C$ air drying oven, add a small amount of sesbania gum powder, mix and knead, squeeze into shape, air dry, and then oven dry. Afterwards, calcine at $350\text{ }^\circ C$ for 4 h to obtain an aluminum oxide type carrier, namely Al_2O_3 . According to ICP-OES measurement, the Na element content of the Al_2O_3 carrier is only 0.0274% (mass fraction). Weigh K_2CO_3 according to the composition ratio of the sample, conduct an incipient wetness of the Al_2O_3 carrier with aqueous solution of K_2CO_3 , and then dry it. Weigh ammonium iron citrate, conduct an incipient wetness again, and then dry it. Then calcine at $350\text{ }^\circ C$ for 4 h to obtain the sample A1 in oxide status.

Preparation of sample A2 (i.e. $15\%Fe + 2\%K_2O + 83\%ZnAl_2O_4$): weigh $Zn(NO_3)_2 \cdot 6H_2O$ and $Al(NO_3)_3 \cdot 9H_2O$ with proper dosage of the nominal composition, add deionized water to dissolve both nitrates into a solution. Weigh $(NH_4)_2CO_3$ and dissolve it in deionized water to form another aqueous solution. The other steps are similar to the corresponding preparation steps of sample A1. According to ICP-OES measurement, the Na element content of the prepared $ZnAl_2O_4$ carrier is only 0.0392% (mass fraction). The obtained sample is sample A2 in oxide status.

Preparation of sample A3 (i.e. $15\%Fe + 2\%K_2O + 83\%ZnAl_2O_4 \cdot Al_2O_3$): The preparation steps are similar to those of sample A2. According to ICP-OES measurement, the Na element content of the prepared $ZnAl_2O_4 \cdot Al_2O_3$ carrier is only 0.0296% (mass fraction). The obtained sample is sample A3 in oxide status.

The oxide status samples A1, A2, and A3 need to be reduced by a gas mixture ($50\%H_2/50\%Ar$ by molar ratio) at $550\text{ }^\circ C$ for 6 h in a tubular furnace or a Fischer–Tropsch reaction apparatus to obtain corresponding freshly reduced samples A1, A2, and A3. More details for the preparation of samples are available in the Supplementary Information.

Characterization

The structure of samples was determined using an X'Pert Pro X-ray powder diffractometer. The elemental compositions of samples were determined using the Elan 9000 inductively coupled plasma mass spectrometer. The pore texture of the sample was measured using a NOVA1000 surface area and pore size analyzer. Use a ChemStar™ chemical adsorption analyzer to determine the surface alkalinity of samples. The morphology of the sample was observed using a QUANTA Q400 field emission electron microscope. More details for the characterization of samples are available in the Supplementary Information.

Catalytic performance tests

Consistent with the testing method in relevant literature [18–20], the catalytic reactions for CO hydrogenation to lower olefins are conducted using a fixed-bed tubular reactor with an internal diameter of 8 mm and unreduced 40–60 mesh catalysts (i.e., in oxide status, 4 mL each). Loaded catalyst is reduced by a pre-mixed gas of 50% H₂/50% Ar at a pressure of 1 atm. Catalysts A1–A3 are activated by reducing in H₂/Ar at 550 °C for 6 h. The in-situ activated catalysts are tested with a pre-mixed syngas (H₂/CO/Ar=45/45/10, by mol%) at a space velocity (SV) of 1500 mL g cat⁻¹ h⁻¹ and a total pressure of 2.0 MPa. Argon is used as the internal standard component of syngas for GC analysis. CO, CH₄ and CO₂ are analyzed by a GC with a TCD detector equipped with a TDX-01 packed column (6 m in length). Incondensable gaseous hydrocarbons are analyzed by a GC with a FID detector equipped with a PLOT Al₂O₃/S (50 m×0.53 mm×25 μm) capillary column. Water phase is analyzed by a GC with a TCD detector equipped with a GDX-102 (2 m×3 mm) packed column. Condensed oil and wax (dissolved in cyclohexane) are analyzed by a GC with a FID detector equipped with an OV-101 (50 m×0.25 mm×0.5 μm) capillary column. Spent catalysts were unloaded from the reactor at room temperature in Ar, stored in glass vials in air, and then tested by XRD in air.

The data processing of conversion and selectivity is based on the amount of carbon atoms in the substance. The CO conversion (x_{CO} , %) is the amount of converted CO divided by the amount of introduced CO. CO₂ selectivity (s_{CO_2} , %) is the amount of CO converted to CO₂ divided by the amount of all converted CO. Hydrocarbon selectivity (s_{HC}) is the percentage of carbon-based substances represented by C₁ (i.e. methane), C₂–C₄, and C₅₊ hydrocarbon (HC) products in the total hydrocarbon products. The olefin/paraffin ratio (O/P) is the molar ratio of the carbon-based substances in olefins to those in alkanes of the same carbon number in hydrocarbons.

Results and discussion

Structure features

Fig. 1 shows the XRD patterns of the samples discharged from the Fischer–Tropsch apparatus after the catalytic reactions, where the structure of a discharged sample is very close to its structure during the reactions. The major crystalline phase of discharged sample A1 is γ -Al₂O₃ (JCPDS 10-0425), while its crystalline phases of iron species are Fe₃O₄ (JCPDS 65-3107) and FeO (JCPDS 06-0615) with weak diffraction peaks, and no diffraction peaks of iron carbide were found. Other iron species in discharged sample A1 is X-ray amorphous.

The major crystalline phase of discharged sample A2 is ZnAl₂O₄ (JCPDS 05-0669), while zinc species also include ZnO (JCPDS 36-1451), indicating that the zinc species have not fully combined with aluminum species, resulting in a small amount of remaining crystalline ZnO and X-ray amorphous Al₂O₃. The crystalline phase of the iron species in discharged sample A2 is Fe₃O₄.

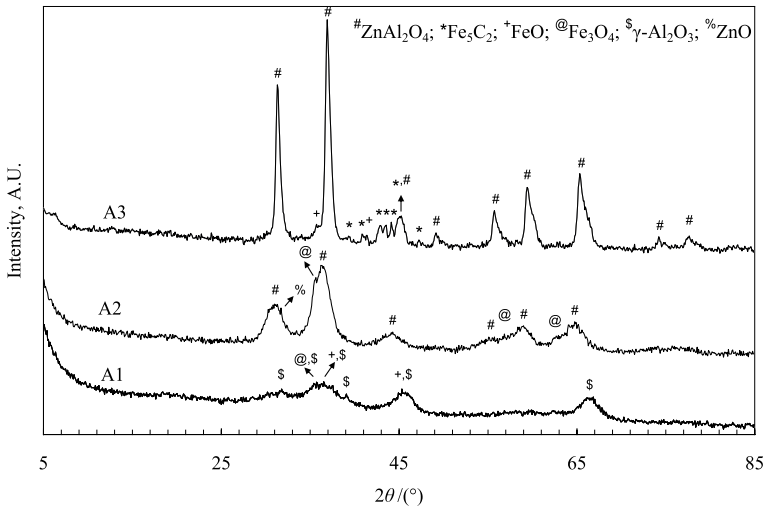


Fig. 1 XRD patterns of discharged samples

The major crystalline phase of discharged sample A3 is also ZnAl_2O_4 . Its other aluminum species is X-ray amorphous Al_2O_3 . The crystalline phases of iron species in discharged sample A3 are Fe_5C_2 (JCPDS 51-0997) and a small amount of FeO .

The XRD pattern of discharged sample A2 shows the presence of ZnO phase, while the XRD pattern of discharged sample A3 does not show the presence of ZnO phase. This indicates that when the nominal composition of the carrier is only ZnAl_2O_4 but there is no Al_2O_3 (i.e. in the case of sample A2), the ZnAl_2O_4 phase in the crystalline phase is not very stable and may partially decompose to produce ZnO and Al_2O_3 . At the same time, it also indicates that when the nominal composition of the carrier includes both ZnAl_2O_4 and Al_2O_3 (in the case of sample A3), the ZnAl_2O_4 phase in the crystalline phase is very stable and will not decompose to ZnO and Al_2O_3 . That is to say, the Al_2O_3 component (except the Al species in ZnAl_2O_4) in the nominal composition of the carrier can effectively inhibit the decomposing reaction of ZnAl_2O_4 phase. It plays a role similar to the principle of Le Chatelier that increasing product concentration can suppress a forward reaction.

Fig. S1 shows the XRD patterns of the freshly reduced samples (i.e., 550°C for 6 h in $50\%\text{H}_2/50\%\text{Ar}$ before catalytic reactions). Each freshly reduced sample won't have the Fe_5C_2 phase because they have not encountered the CO molecules yet. The reduced iron phase in these three samples is not Fe^0 (JCPDS 06-0696) but FeO , verifying that the iron species in them are not thoroughly reduced. The order of XRD peak intensity of FeO phase from strong to weak is $\text{A3} > \text{A2} > \text{A1}$, indicating that the iron species of sample A3 is most easily to be reduced, while that of sample A1 is the most difficult to be reduced. Combining above analysis, one may find that iron species supported on $(\text{ZnAl}_2\text{O}_4\text{-Al}_2\text{O}_3)$ composite carrier is more prone to be reduced during the reduction process than on ZnAl_2O_4 carrier and Al_2O_3 carrier, and is also more prone to carbonization and formation of iron

carbide in subsequent catalytic reactions. The XRD analysis results are consistent with those in analogous studies from the literature [18–20].

Texture features

The N_2 physical adsorption–desorption result of the freshly reduced sample A3 is shown in Fig. 2 and Fig. S2. From Fig. 2a and Fig. S2a, it can be seen that the N_2 adsorption–desorption isotherm of this sample belongs to type IV of IUPAC classification, indicating that this sample belongs to mesoporous adsorbent [22]. Its hysteresis loop can be classified as H3 type, indicating that this sample has narrow slit shaped pores formed by the aggregation of layered (or plate-like) particles [22]. The mesoporosity is calculated by the BJH method [22] using the adsorption branch of isotherm plot. Fig. 2b and Fig. S2b show that this sample has micropores ranging from 1.2 to 1.9 nm, mesopores ranging from 2.1 to 44.4 nm, and macropores ranging from 70.8 to 134.6 nm. The BET specific surface area of this sample is $46.6 \text{ m}^2 \text{ g}^{-1}$, the single point total pore volume is $0.362 \text{ cm}^3 \text{ g}^{-1}$, and the average pore diameter is 31.0 nm.

Electron microscopy studies

Fig. 3 shows the FESEM images of the freshly reduced sample A3. As shown in Fig. 3c, the sample consists of two types of particles. One is a layered particle with a width of approximately 0.2–2.0 μm which belongs to the carrier $\text{ZnAl}_2\text{O}_4\cdot\text{Al}_2\text{O}_3$ phase, as aluminum-containing oxides often exhibit a layered microstructure [18, 19]. The other type is a mixture of iron and potassium species, consisting of approximately spherical small particles with a diameter of approximately 10–40 nm, carried on the surface of layered particles. Fig. 3b shows that these layered carrier particles aggregate into a stacking structure, with rich stacking layers, strong three-dimensional sense, and relatively dense stacking degree. The stacking structures formed by these layered particles can generate pores with different shapes.

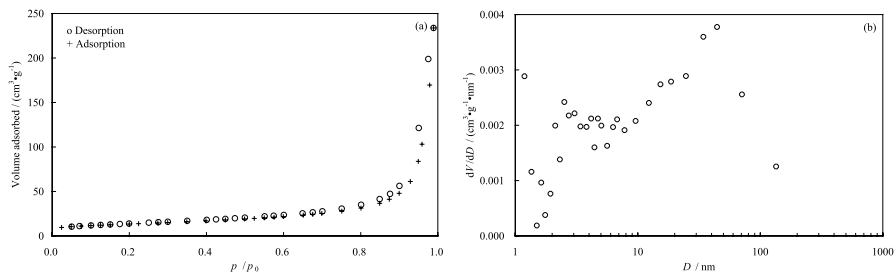
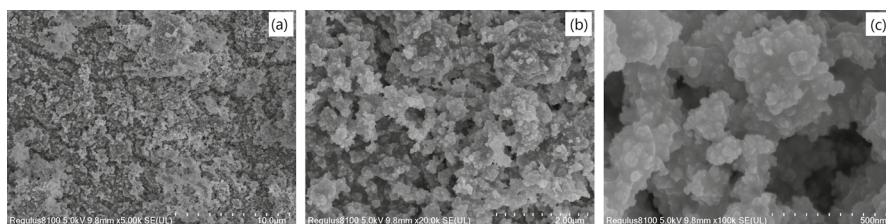


Fig. 2 Physical adsorption isotherm and pore diameter distribution of sample A3. **a** Isotherm plot; **b** BJH pore diameter distribution



(a) sample A3 magnified by 5000 times; (b) sample A3 magnified by 20000 times; (c) sample A3 magnified by 100000 times

Fig. 3 FESEM images of sample A3. **a** sample A3 magnified by 5000 times; **b** sample A3 magnified by 20,000 times; **c** sample A3 magnified by 100,000 times

Surface alkalinity of samples

Software OriginPro 2019b is employed for the curve fitting of CO₂-TPD results, which is a universal analytical method and has been used in our previous reports [18–20]. Fig. 4 shows the CO₂-TPD curves of three freshly reduced samples, and the corresponding curve integration data are listed in Table 1. The low-temperature desorption peak refers to the low-temperature region desorption peak with the peak position below 300 °C, the medium-temperature desorption peak is the intermediate temperature region desorption peak between 300 and 600 °C, and the high-temperature desorption peak is the high-temperature region desorption peak above 600 °C.

From Fig. 4, it can be seen that the CO₂-TPD curves of samples A1 and A2 have similar shapes, with desorption peaks in both the low-temperature and high-temperature regions, and the desorption peaks in the low-temperature region are significantly larger than those in the high-temperature region. However, the CO₂-TPD curve of sample A3 showed no desorption peaks in both the

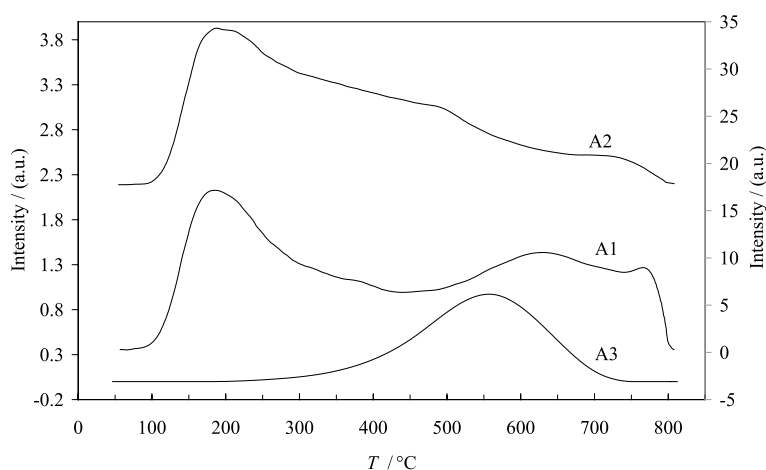


Fig. 4 CO₂-TPD profiles of samples (Curves A1 and A2 both follow the right Y axis, while curve A3 follows the left Y axis.)

Table 1 Integral data of CO₂-TPD results of Fig. 4

Catalyst code	Low-temperature desorption peak (< 300°C)			Medium-temperature desorption peak (300–600°C)			High-temperature desorption peak (> 600°C)			A_{total}
	$T/^\circ\text{C}$	A_{low}	$R_{\text{low}}/\%$	$T/^\circ\text{C}$	A_{medium}	$R_{\text{medium}}/\%$	$T/^\circ\text{C}$	A_{high}	$R_{\text{high}}/\%$	
A1	185	3479	53	— ^a	—	—	629 766	2608 445	40 7	6532
A2	188	4199	74	494	1171	21	672	308	5	5678
A3	—	—	—	555	202	100	—	—	—	202

A_{total} , total integral area; A_{high} , integral area of high-temperature desorption peak; A_{medium} , integral area of medium-temperature desorption peak; A_{low} , integral area of low-temperature desorption peak; R_{high} , $(A_{\text{high}}/A_{\text{total}}) \times 100\%$; R_{medium} , $(A_{\text{medium}}/A_{\text{total}}) \times 100\%$; R_{low} , $(A_{\text{low}}/A_{\text{total}}) \times 100\%$

^aNo data

low and high temperature regions, with only weak medium-temperature desorption peak in the intermediate temperature region. These properties indicate that the catalytic properties of samples A1 and A2 may be similar, while the catalytic properties of sample A3 will be significantly different from those of samples A1 and A2.

From Table 1 and Fig. 4, it can be seen that the sequence of the total integrated area (A_{total}) of the CO₂-TPD curves from large to small is A1(6532 A.U.) > A2(5678) > A3(202), indicating that the sequence of the total quantity of base sites on the sample surface from large to small is A1 > A2 > A3. The order of the integral area of the high-temperature desorption peaks from large to small is also A1 > A2 > A3, indicating that the order of the surface alkalinity of the samples from strong to weak is also A1 > A2 > A3. The characteristic of sample A1 is that the surface weak base sites and strong base sites are almost half, accounting for 53% and 47%, and its total quantity of base sites is the highest. The characteristic of sample A2 is that the quantity of weak base sites (74%) > the quantity of moderate base sites (21%) > the quantity of strong base sites (5%), and its total quantity of base sites is only a little less than sample A1. The characteristic of sample A3 is that it has and only has moderate base sites (accounting for 100%), and its quantity of base sites is much smaller than samples A1 and A2.

The surface alkalinity derived from carriers and/or electronic promoters has a significant impact on the CO hydrogenation performance of a sample. For example, potassium promoter (usually abbreviated as K₂O or K) is commonly used in the CO hydrogenation process with iron catalysts. K₂O promoter can act as electron donors to push electrons towards the iron active center, enhance the strength of the Fe–C bond, promote the chemical adsorption of CO molecules, and adjust the reaction rate of CO hydrogenation. At the same time, K₂O promoter can reduce the heat of H₂ adsorption, reduce the coverage of H₂ adsorption, and play a role in inhibiting hydrogenation and increasing the olefin/paraffin ratio [23].

Catalytic performance tests

Catalytic activity

The reaction performance data of the catalyst samples are shown in Tables 2, 3, 4 and Figs. S3–S10. Supporting Information Fig. S3a shows the CO conversion at different reaction temperatures, while Supporting Information Fig. S3b shows the iron time yield at different reaction temperatures. Iron time yield (FTY) represents moles of CO converted to hydrocarbons per unit of Fe per second.

According to the commonly used comparison method of catalyst activity by half conversion [18–20], as shown in Supporting Information Fig. S3a, the sequence of the Fischer–Tropsch reaction activity of the samples from high to low is $A_3 > A_2 > A_1$, and the difference in sample activity between A_2 and A_1 is not significant. The activity sequence of these samples shows an inverse relationship with the total desorption peak area (A_{total}) of CO_2 -TPD, as well as with the desorption peak area in the medium/high temperature region ($A_{\text{medium}} + A_{\text{high}}$) of CO_2 -TPD. However, this activity sequence has no significant relationship with the desorption peak area in the low-temperature region (A_{low}). These phenomena indicate that the desorption peak area in the medium/high temperature region determines the activity of a sample, while the desorption peak area in the low-temperature region lacks a significant impact on the activity of a sample. That is to say, the quantity of base sites with moderate or higher alkalinity determines the activity of the sample and is inversely related to the activity of a sample. The quantity of weak base sites lacks significant impact on the activity of a sample. Therefore, it can be inferred that the stronger the alkalinity on the surface of a sample, the stronger the inhibitory effect on the activity of this sample.

Above phenomenon is consistent with the literature [18, 19] about Fe/K supported on 1200 °C-annealed Al–O–Zn carriers, which can be deduced that the catalytic activity is negatively correlated with the strength of stronger basicity sites of the catalysts. This phenomenon is also consistent with the theory of Maitlis et al. [24], because the neutralization of the Lewis acidity of a support by a base may weaken the activation of CO molecules and thus slow down the reaction rate. This research result is also consistent with the result of Prieto et al., which suggests that basic oxide may significantly lower down CO hydrogenation rate via a “selective blockage” of some sites on transition metal which are important for CO hydrogenation [25, 26].

CO_2 selectivity

Due to the different activity of each sample, the reaction temperature range varies greatly. Therefore, the following Figures not only show the trend of selectivity with temperature (i.e., panel a of each figure), but also the trend of selectivity with CO conversion (i.e., panel b of each figure). CO_2 is an inevitable product of the Fischer–Tropsch reaction, and its selectivity is generally not higher than 50% [18]. As shown in Tables 2, 3, 4 and Supporting Information Fig. S4, the CO_2 selectivity data of samples A_1 and A_2 follow this pattern, both below 50%. The CO_2 selectivity of

Table 2 Catalytic performance of catalyst A1

T (°C)	X_{CO} (%)	S_{CO_2} (%)	Hydrocarbon selectivity (%)							Olefin/paraffin ratio					FTY (10^{-5} mol _{CO} / g _{Fe} s)
			C_1	C_2	C_3	C_4	C_2-C_4	C_{3+}	C_1-C_4	C_2-C_4	C_2	C_3	C_4	C_2-C_4	
310	6.25	44.76	37.59	21.61	23.53	12.98	58.12	4.29	95.71	15.65	0.03	0.55	1.08	0.37	0.54
320	12.28	47.30	38.94	21.92	22.79	12.06	56.77	4.28	95.72	13.66	0.02	0.46	1.01	0.32	1.05
330	21.12	47.18	41.90	22.25	21.40	10.78	54.44	3.67	96.33	11.41	0.02	0.37	0.90	0.27	1.81
340	30.00	45.28	41.27	23.10	21.53	10.60	55.23	3.50	96.50	10.90	0.02	0.34	0.87	0.25	2.57
350	46.18	48.08	43.84	24.16	20.65	8.99	53.80	2.36	97.64	10.34	0.03	0.35	0.89	0.24	3.96
360	61.13	48.70	43.32	25.27	19.95	8.57	53.79	2.88	97.12	9.80	0.03	0.33	0.86	0.22	5.24
370	65.18	46.89	42.26	25.95	20.48	8.91	55.33	2.40	97.60	9.00	0.03	0.28	0.75	0.19	5.58
380	70.09	47.09	42.51	26.37	20.27	8.54	55.19	2.30	97.70	8.68	0.03	0.27	0.69	0.19	6.01
390	73.15	46.83	42.78	26.67	20.27	8.15	55.09	2.13	97.87	8.92	0.04	0.30	0.67	0.19	6.27

Catalyst A1: 15%Fe/2%K₂O/83%Al₂O₃, $P = 2.0$ MPa, $SV = 1500$ mL g cat⁻¹ h⁻¹. $n(H_2)$: $n(CO)$: $n(Ar) = 45:45:10$. Iron time yield (FTY) represents moles of CO converted to hydrocarbons per unit of Fe per second

Table 3 Catalytic performance of catalyst A2

T ($^{\circ}\text{C}$)	X_{CO} (%)	S_{CO_2} (%)	Hydrocarbon selectivity (%)							Olefin/paraffin ratio				FTY (10^{-5} mol _{CO} / g _{Fe} s)	
			C_1	C_2	C_3	C_4	$\text{C}_2\text{-C}_4$	C_{5+}	$\text{C}_1\text{-C}_4$	$\text{C}_2\text{-C}_4$	C_2	C_3	C_4		$\text{C}_2\text{-C}_4$
330	7.39	46.09	52.54	21.27	15.80	7.24	44.31	3.15	96.85	7.44	0.06	0.30	0.54	0.20	0.63
340	16.67	46.77	52.81	21.67	15.70	7.01	44.37	2.81	97.19	7.81	0.06	0.34	0.57	0.21	1.43
350	48.32	44.06	44.79	18.28	13.06	5.68	37.02	18.19	86.73	6.05	0.05	0.29	0.54	0.18	4.14
360	63.35	42.87	43.44	18.67	12.93	5.43	37.03	19.53	80.47	5.02	0.04	0.25	0.48	0.16	5.43
370	80.74	41.78	39.35	21.33	16.41	6.73	44.48	16.17	83.83	4.15	0.02	0.15	0.30	0.10	6.92

Catalyst A2: 15%Fe/2%K₂O/83%ZnAl₂O₄. $P = 2.0$ MPa. $SV = 1500$ mL g cat⁻¹ h⁻¹. $n(\text{H}_2)$: $n(\text{CO}) = 45:45:10$. Iron time yield (FTY) represents moles of CO converted to hydrocarbons per unit of Fe per second

Table 4 Catalytic performance of catalyst A3

T ($^{\circ}\text{C}$)	X_{CO} (%)	S_{CO_2} (%)	Hydrocarbon selectivity (%)							Olefin/paraffin ratio				FTY (10^{-5} mol _{CO} / g _{Fe} s)	
			C_1	C_2	C_3	C_4	$\text{C}_2\text{-C}_4$	C_{3+}	$\text{C}_1\text{-C}_4$	$\text{C}_2\text{-C}_4$	$\text{C}_2\text{-C}_4$	C_2	C_3		C_4
300	6.86	63.29	34.55	24.76	25.65	10.00	60.40	5.05	94.95	41.63	1.01	4.49	4.70	2.22	0.59
305	17.93	58.12	29.90	22.94	24.80	13.62	61.36	8.74	91.26	42.57	1.01	4.06	4.47	2.27	1.54
310	38.16	61.15	28.96	22.81	24.70	14.36	61.87	9.17	90.83	43.93	1.08	4.36	5.00	2.45	3.27
315	66.29	62.19	29.53	25.46	25.87	12.28	63.60	6.87	93.13	44.67	1.04	4.75	5.23	2.36	5.68
320	78.48	58.77	29.16	25.11	26.92	12.02	64.04	6.80	93.20	42.21	0.73	4.22	4.57	1.93	6.72
330	83.90	57.37	32.18	25.74	25.54	10.46	61.74	6.09	93.91	37.16	0.53	3.54	3.93	1.51	7.19

Catalyst A3: 15%Fe/2%K₂O/83%ZnAl₂O₄·Al₂O₃; $P=2.0$ MPa, $SV=1500$ mL g cat⁻¹ h⁻¹, $n(\text{H}_2)$: $n(\text{CO})=45:45:10$. Iron time yield (FTY) represents moles of CO converted to hydrocarbons per unit of Fe per second

A2 is slightly lower than that of A1. The CO₂ selectivity of sample A3 is higher than 50%, indicating that this sample may have a little higher water–gas shift activity [18]. The CO₂ selectivity of these samples is positively correlated with the ratio of desorption peak area in the medium/high temperature region ($R_{\text{medium}} + R_{\text{high}}$). This ratio ($R_{\text{medium}} + R_{\text{high}}$) represents the percentage of base sites with moderate or higher strength in the sum of all surface base sites. The lower the value of this ratio, the more weak base sites tend to dominate. The higher the value of this ratio, the more dominant the moderate/strong base sites tend to be.

Hydrocarbon selectivity (C₅₊)

Theoretically, heating up will lower down the C₅₊ hydrocarbon selectivity. The reason for this rule is that the desorption rate of intermediates will accelerate during the increase of reaction temperature, which will reduce the chances of forming longer carbon chains. As shown in Tables 2, 3, 4 and Supporting Information Fig. S5, the important property of these samples lies in that their C₅₊ hydrocarbon selectivity data are all below 20%, and the C₅₊ hydrocarbon selectivity data of samples A1 and A3 are even lower than 10%, indicating that all three samples have the property of inhibiting C–C coupling.

The trend of C₅₊ hydrocarbon selectivity in samples A2 and A3 rises with increasing temperature in their lower reaction temperature ranges, and then lowers down with further temperature increase in their higher reaction temperature ranges. This indicates that in their lower reaction temperature ranges, the C₅₊ hydrocarbon selectivity of samples A2 and A3 is dominated by their own inhibition of C–C coupling properties. However, as the temperature gradually increases in their lower reaction temperature ranges, the inhibition of C–C coupling properties of samples A2 and A3 will be gradually weaken, leading to a gradual increase in C₅₊ hydrocarbon selectivity.

After the C₅₊ hydrocarbon selectivity reaches its highest point, samples A2 and A3 enter their higher reaction temperature ranges. In these higher temperature ranges, the influence of temperature has completely surpassed the influence of the sample's own properties and begins to dominate. Therefore, the C₅₊ hydrocarbon selectivity trend of samples A2 and A3 shifts to decrease with the increase of temperature.

The C₅₊ hydrocarbon selectivity of sample A1 gradually decreases with the increase of temperature, which is consistent with above mentioned theoretical rule. However, it does not indicate that the reaction temperature plays a dominant role in the entire process of C₅₊ hydrocarbon selectivity of sample A1. Because the C₅₊ hydrocarbon selectivity of sample A1 is lower than 5% even at the lowest reaction temperature and is only 2% at the highest reaction temperature, which is at an extremely low level throughout the entire process, this actually means that sample A1 itself has extremely strong properties in inhibiting C–C coupling. Therefore, sample A1 did not show a significant increase and then decrease in C₅₊ hydrocarbon selectivity as in the other two samples, which may be due to its surface having particularly strong base sites (i.e., desorption temperature up to 766 °C in CO₂-TPD).

Hydrocarbon selectivity (C_1 – C_4)

Tables 2, 3, 4 and Fig. S6 show the trend of C_1 – C_4 hydrocarbon selectivity in the samples. C_{5+} is the hydrocarbons with longer carbon chains, while C_1 – C_4 is the hydrocarbons with shorter carbon chains, and the sum of the two is equal to 100%. The stronger the sample's ability to suppress C–C coupling, the higher the C_1 – C_4 hydrocarbon selectivity. The variation trend of C_1 – C_4 hydrocarbon selectivity is the horizontal axis mirror image of the variation trend of C_{5+} hydrocarbon selectivity.

Hydrocarbon selectivity (CH_4)

Tables 2, 3, 4 and Fig. S7 show the trend of CH_4 hydrocarbon selectivity in the samples. CH_4 is the C_1 in C_1 – C_4 hydrocarbons, and its hydrocarbon selectivity value is a part of the C_1 – C_4 hydrocarbon selectivity value, which is inevitably significantly influenced by the latter, that is, by the sample's property of inhibiting C–C coupling. Meanwhile, CH_4 is also a completely hydrogenated product, which will be inevitably influenced by the hydrogenation property of the sample. Among the three samples, sample A3 has the lowest selectivity for CH_4 hydrocarbons, while its selectivity for C_1 – C_4 hydrocarbons is not the lowest. Therefore, the hydrogenation property of sample A3 must be the mildest among the three samples. The CH_4 hydrocarbon selectivity data of samples A1 and A2 are higher than sample A3, indicating that their hydrogenation properties are stronger than sample A3.

Hydrocarbon selectivity (C_2 – C_4)

Tables 2, 3, 4 and Fig. S8 show the trend of C_2 – C_4 hydrocarbon selectivity in the samples. C_2 – C_4 hydrocarbons are a part of C_1 – C_4 hydrocarbons. Due to the fact that the C_1 – C_4 hydrocarbon selectivity of sample A1 is generally the highest among the three, it seems that A1 should also have the highest C_2 – C_4 hydrocarbon selectivity. However, due to its significantly higher CH_4 hydrocarbon selectivity than sample A3, A1 does not actually have the highest C_2 – C_4 hydrocarbon selectivity. Although the C_1 – C_4 hydrocarbon selectivity of sample A3 did not reach the highest value among the three, its CH_4 hydrocarbon selectivity was lower than A1 and A2, resulting in A3 having the highest C_2 – C_4 hydrocarbon selectivity among the three.

C_2 – C_4 olefin/paraffin ratio

Tables 2, 3, 4 and Fig. S9 show the trend of the C_2 – C_4 olefin/paraffin ratio of the samples. The primary reaction product of CO hydrogenation is not alkanes, but linear 1-*n*-alkenes. The linear 1-*n*-alkenes generated by the primary reaction can continue to undergo secondary reactions on the surface of the sample, generating alkanes [26]. The order of the C_2 – C_4 olefin/paraffin ratio of the three samples from high to low is $A3 > A1 > A2$. The ratio of the desorption peak area ($R_{\text{medium}} + R_{\text{high}}$) in the medium/high temperature region of the three samples also ranges from high to low in the order of $A3(100\%) > A1(47\%) > A2(26\%)$. Therefore, similar to the CO_2 selectivity, the C_2 – C_4 olefin/paraffin ratio of these samples also shows a positive

relationship with the proportion of desorption peak area ($R_{\text{medium}} + R_{\text{high}}$) in the medium/high temperature region. Having a simple moderate strength surface base site (such as sample A3) seems more suitable for mild hydrogenation than having other (weak, strong) base sites (such as those in samples A1 and A2). Structurally speaking, XRD results show that only A3 of the three samples contains a certain amount of Fe_5C_2 crystalline phase. The literature indicates that the characteristic of iron carbide is mild hydrogenation [4, 11], so sample A3 exhibits significantly different CO_2 -TPD characteristics from A1 and A2, and has a higher C_2 - C_4 olefin/paraffin ratio than A1 and A2.

Hydrocarbon selectivity ($\text{C}_2^=-\text{C}_4^=$)

Tables 2, 3, 4 and Fig. S10 show the trend of $\text{C}_2^=-\text{C}_4^=$ hydrocarbon selectivity of the samples. The hydrocarbon selectivity of lower olefins not only has a positive relationship with the C_2 - C_4 hydrocarbon selectivity, but also with the C_2 - C_4 olefin/paraffin ratio. Therefore, due to the fact that sample A3 not only has the highest C_2 - C_4 hydrocarbon selectivity, but also has the highest C_2 - C_4 olefin/paraffin ratio among the three samples, the $\text{C}_2^=-\text{C}_4^=$ hydrocarbon selectivity of sample A3 is significantly higher than that of A1 and A2.

As shown in Fig. S10b, under similar conversions (i.e., $x_{\text{CO}} = \text{ca. } 63\text{--}66\%$), when the nominal composition of the carrier is Al_2O_3 (i.e., sample A1) or ZnAl_2O_4 (i.e., sample A2), the obtained $\text{C}_2^=-\text{C}_4^=$ hydrocarbon selectivity is 9% or 5%, respectively. When the nominal composition of the carrier is a simple combination of Al_2O_3 and ZnAl_2O_4 (i.e., the $\text{ZnAl}_2\text{O}_4 \cdot \text{Al}_2\text{O}_3$ carrier in sample A3), the obtained $\text{C}_2^=-\text{C}_4^=$ hydrocarbon selectivity can reach 45%, which is 5 and 9 times higher than samples A1 and A2, respectively. This is a typical synergistic effect based on carrier composition, which is highly worthy of further research. The basis for this synergistic effect is a significant change on the surface base sites of the samples, which means that the surface base characteristic of sample A3 becomes significantly different from that of sample A1 or A2.

In addition, it would be more beneficial to compare the catalytic activity of the catalysts in the study with the activities of other catalysts studied in the literature on a similar subject. This comparison has been presented in tabular form as Supporting Information Table S1. Furthermore, reusability is particularly important for industrial applications. Therefore, our future work may focus on the topics related, such as characterization of the spent catalysts and other issues leading to catalyst deactivation (such as coke formation, catalyst sintering, etc.) as well as catalyst regeneration.

Conclusions

Three Fe/K catalyst samples supported by different carriers were prepared using ammonium carbonate as a sodium free precipitant and under mild calcination condition at 350 °C. Iron species on ($\text{ZnAl}_2\text{O}_4 \cdot \text{Al}_2\text{O}_3$) composite carrier is more prone to reduction and carbonization than on ZnAl_2O_4 carrier or Al_2O_3 carrier. All three samples exhibited the property of inhibiting C-C coupling. The stronger the alkalinity

on the surface of a sample, the stronger the inhibitory effect on the activity of the sample. Both CO₂ selectivity and C₂–C₄ olefin/paraffin ratio of a sample exhibit a positive relationship with the proportion of desorption peak area ($R_{\text{medium}} + R_{\text{high}}$) in the medium/high temperature region. For samples with relatively weaker surface alkalinity (i.e., samples A2 and A3), the surface alkalinity plays a dominant role in product selectivity in the lower reaction temperature range, while in the higher reaction temperature range, it gradually becomes the reaction temperature itself who dominates. For the sample with relatively stronger surface alkalinity (i.e., sample A1), only the surface alkalinity of the sample plays a dominant role in the entire process of product selectivity in the entire reaction temperature range, while the effect of reaction temperature on product selectivity is very limited. Having a simple moderate strength surface base site is more suitable for mild hydrogenation than having other (weak, strong) base sites. When the conversion is similar (i.e., $x_{\text{CO}} = \text{ca. } 63\text{--}66\%$), the C₂–C₄ hydrocarbon selectivity of the prepared (ZnAl₂O₄, Al₂O₃) composite supported Fe/K sample (A3) can reach 5 times that of the prepared Al₂O₃ supported Fe/K sample (A1) and 9 times that of the prepared ZnAl₂O₄ supported Fe/K sample (A2), showing a typical synergistic effect based on carrier composition. The basis for the synergistic effect is that the surface base sites of sample A3 exhibit significantly different characteristic compared to samples A1 and A2, which may be related to the relatively high content of Fe₃C₂ crystalline phase in sample A3.

Supplementary Information The online version contains supplementary material available at <https://doi.org/10.1007/s11144-023-02555-0>.

Acknowledgements We thank the National Natural Science Foundation of China (NSFC, No. 21571161) and Fundamental Research Fund Project of Zhengzhou University of Light Industry (CLY-LiuZhenxin) for financial support.

Declarations

Conflict of interest The authors declare that they have no conflict of interest.

References

1. Zhao B, Huang X, Ding Y, Bi Y (2023) Bias-free solar-driven syngas production: a Fe₂O₃ photoanode featuring single-atom cobalt integrated with a silver-palladium cathode. *Angew Chem Int Ed*. <https://doi.org/10.1002/anie.202213067>
2. Wang Z-H, Cao J-P, Tang W, He Z-M, Yang F-L, Wang Z-Y, Zhao X-Y (2023) Facile synthesis of low-cost Co-Cu/C alloy catalysts for hydrogen-rich syngas production from low-temperature steam reforming of biomass tar. *Chem Eng Sci*. <https://doi.org/10.1016/j.ces.2022.118370>
3. Okonye LU, Yao Y, Ren J, Liu X, Hildebrandt D (2023) A perspective on the activation energy dependence of the Fischer-Tropsch synthesis reaction mechanism. *Chem Eng Sci*. <https://doi.org/10.1016/j.ces.2022.118259>
4. Duan Y, Zhang W, Sun H, Lu W. (2023) Adsorption and activation of CO on perfect and defective *h*-Fe₃C₃ surfaces for Fischer-Tropsch synthesis. *Mol Catal* 541: <https://doi.org/10.1016/j.mcat.2023.113081>
5. Khasu M, Marquart W, Kooyman PJ, Drivas C, Isaacs MA, Mayer AJ, Dann SE, Kondrat SA, Claeys M, Fischer N (2023) Empowering catalyst supports: a new concept for catalyst design demonstrated in the Fischer-Tropsch synthesis. *ACS Catal* 13:6862–6872

6. Han X, Huang S, Ma X (2023) Interface-induced phase evolution and spatial distribution of Fe-based catalysts for Fischer-Tropsch synthesis. *ACS Catal* 13:6525–6535
7. Zhao Z, Li Y, Zhu H, Yuan L, Ding Y (2023) A review of Co/Co₂C-based catalysts in Fischer-Tropsch synthesis: from fundamental understanding to industrial applications. *Chem Commun* 59:3827–3837
8. Zhang B, Yao J, Wang Y, Gao W, Kugue Y, Guo X, He Y, Yang G, Tsubaki N (2023) Effects of zeolite morphologies on CO conversion to aromatics via a modified Fischer-Tropsch synthesis pathway. *J Chem Technol Biotechnol* 98:98–105
9. Kern C, Jess A (2023) Improvement of a multi-tubular Fischer-Tropsch reactor with gas recycle by appropriate combination of axial activity distribution and gas velocity. *Catal Sci Technol* 13:2212–2222
10. Zhou W, Cheng K, Kang J, Zhou C, Subramanian V, Zhang Q, Wang Y (2023) New horizon in C1 chemistry: breaking the selectivity limitation in transformation of syngas and hydrogenation of CO₂ into hydrocarbon chemicals and fuels. *Chem Soc Rev* 48(5):3193–3228
11. Torres Galvis HM, Bitter JH, Ruitenbeek M, de Jong KP (2012) Supported iron nanoparticles as catalysts for sustainable production of lower olefins. *Science* 335:835–838
12. Torres Galvis HM, Koeken ACJ, Bitter JH, Davidian T, Ruitenbeek M, Dugulan AI, de Jong KP (2013) Effects of sodium and sulfur on catalytic performance of supported iron catalysts for the Fischer-Tropsch synthesis of lower olefins. *J Catal* 303:22–30
13. Xu Y, Li X, Gao J, Wang J, Ma G, Wen X, Yang Y, Li Y, Ding M (2021) A hydrophobic FeMn@Si catalyst increases olefins from syngas by suppressing C₁ by-products. *Science* 371:610–613
14. Zhong L, Yu F, An Y, Zhao Y, Sun Y, Li Z, Lin T, Lin Y, Qi X, Dai Y, Gu L, Hu J, Jin S, Shen Q, Wang H (2016) Cobalt carbide nanoprisms for direct production of lower olefins from syngas. *Nature* 538:84–87
15. Jiao F, Li J, Pan X, Xiao J, Li H, Ma H, Wei M, Pan Y, Zhou Z, Li M, Miao S, Li J, Zhu Y, Xiao D, He T, Yang J, Qi F, Fu Q, Bao X (2016) Selective conversion of syngas to light olefins. *Science* 351:1065–1068
16. Cheng K, Gu B, Liu XL, Kang JC, Zhang QH, Wang Y (2016) Direct and highly selective conversion of synthesis gas into lower olefins: Design of a bifunctional catalyst combining methanol synthesis and carbon-carbon coupling. *Angew Chem Int Ed* 55:4725–4728
17. Yu Y, Xu Y, Cheng D, Chen Y, Chen F, Lu X, Huang Y, Ni S (2014) Transformation of syngas to light hydrocarbons over bifunctional CuO-ZnO/SAPO-34 catalysts: the effect of preparation methods. *React Kinet Mech Catal* 112:489–497
18. Liu Z, Jia G, Zhao C, Xing Y (2021) Selective iron catalysts for direct Fischer-Tropsch synthesis to light olefins. *Ind Eng Chem Res* 60:6137–6146
19. Liu Z, Jia G, Zhao C, Xing Y (2023) Effective Fe/K catalyst for Fischer-Tropsch to light alkenes. *Catal Lett*. Article in Press. <https://doi.org/10.1007/s10562-023-04296-0>
20. Xing Y, Guo X, Jia G, Fang S, Zhao C, Liu Z (2020) Investigations on the Zn/Fe ratio and activation route during CO hydrogenation over porous iron/spinel catalysts. *React Kinet Mech Catal* 129:755–772
21. Xing Y, Liu Z, Xue Y, Wu D, Fang S (2016) Variation trends of CO hydrogenation performance of (Al)-O-(Zn) supported cobalt nanocomposites: Effects of gradual doping with Zn-O Lewis base. *Catal Lett* 146:682–691
22. Sing KSW, Everett DH, Haul RAW, Moscou L, Pierotti RA, Rouquerol J, Simmieniewska T (1985) Reporting physisorption data for gas/solid systems with special reference to the determination of surface area and porosity (Recommendations 1984). *Pure Appl Chem* 57:603–619
23. Dry ME, Shingles T, Boshoff LJ, Oosthuizen GJ (1969) Heats of chemisorption on promoted iron surfaces and the role of alkali in Fischer-Tropsch synthesis. *J Catal* 15:190–199
24. Maitlis PM, Zanotti V (2009) The role of electrophilic species in the Fischer-Tropsch reaction. *Chem Commun* 13:1619–1634
25. Prieto G, De Mello MIS, Concepción P, Murciano R, Pergher SBC, Martínez A (2015) Cobalt-catalyzed Fischer-Tropsch synthesis: chemical nature of the oxide support as a performance descriptor. *ACS Catal* 5:3323–3335
26. Turner ML, Marsih N, Mann BE, Quyoum R, Long HC, Maitlis PM (2002) Investigations by ¹³C NMR spectroscopy of ethene-initiated catalytic CO hydrogenation. *J Am Chem Soc* 124:10456–10472

Publisher's Note Springer Nature remains neutral with regard to jurisdictional claims in published maps and institutional affiliations.

Springer Nature or its licensor (e.g. a society or other partner) holds exclusive rights to this article under a publishing agreement with the author(s) or other rightsholder(s); author self-archiving of the accepted manuscript version of this article is solely governed by the terms of such publishing agreement and applicable law.